Three-dimensional two-phase flow model of proton exchange membrane fuel cell with parallel gas distributors

Xunliang Liu*, Guofeng Lou, Zhi Wen

School of Mechanical Engineering, University of Science and Technology Beijing, Beijing 100083, PR China

ABSTRACT

A non-isothermal, steady-state, three-dimensional (3D), two-phase, multicomponent transport model is developed for proton exchange membrane (PEM) fuel cell with parallel gas distributors. A key feature of this work is that a detailed membrane model is developed for the liquid water transport with a two-mode water transfer condition, accounting for the non-equilibrium humidification of membrane with the replacement of an equilibrium assumption. Another key feature is that water transport processes inside electrodes are coupled and the balance of water flux is insured between anode and cathode during the modeling. The model is validated by the comparison of predicted cell polarization curve with experimental data. The simulation is performed for water vapor concentration field of reactant gases, water content distribution in the membrane, liquid water velocity field and liquid water saturation distribution inside the cathode. The net water flux and net water transport coefficient values are obtained at different current densities in this work, which are seldom discussed in other modeling works. The temperature distribution inside the cell is also simulated by this model.

© 2009 Elsevier B.V. All rights reserved.

1. Introduction

Proton exchange membrane (PEM) fuel cells are supposed to be the most promising candidate for powering of electric vehicles due to their high power density, short response time, low operating temperature and pollution free. Modeling and simulation are being used extensively in researches and industrial applications across the world to gain better understanding of the fundamental processes and to optimize fuel cell designs before building a prototype for engineering application.

The importance of water management to PEM fuel cell performance is repeatedly expressed in the early published work [1–5]. Despite several studies on water management in the cell within the past decade, effective water management has remained imperfect. This is partly due to the fact that liquid water is transported within the membrane-electrode-assembly (MEA) by the several coexisting and comparable forces. They are electro-osmotic drag due to the electrical potential, back diffusion from the cathode due to nonuniform concentration, diffusion and hydraulic permeation due to the pressure difference. The other complication results from the conflict that while liquid water is necessary to ensure good ionic

conductivity of the membrane, excessive water can result in flooding of the electrodes at high current. Thus it is neither desirable to remove the water completely, nor is it desirable to have excessive water. The difficulty of water management exists in this.

Over the past few years, some modeling works of liquid water formation and transport were published in the literature. Baschuk and Li [6] proposed the one-dimensional steady-state model in which the degree of water flooding was determined by matching the predictions to the experimental polarization curve. He et al. [7] developed a two-dimensional (2D) two-phase model for cathode of PEM fuel cell with interdigitated flow field. The model included capillary transport of liquid water in a completely wetted gas diffusion layer (GDL). Wang et al. [8] classified four regimes of water transport in the PEMFC air cathode and presented a 2D two-phase flow model based on the multiphase mixing model (M^2 model) formulation of Wang and Cheng [9]. Subsequently, You and Liu [10] published a similar work investigating the effects of several operating parameters on two-phase transport. Berning and Djilali [11] developed a non-isothermal water transport model, in their work, the water formed at the cathode catalyst layer (CL) by electrochemical reactions was assumed to be in the liquid phase and any phase-change phenomena was neglected. The works of Van Zee and co-workers [12,13] have introduced water transport models, in which phase change is assumed to occur only at the interface between the membrane and the electrode, and two-phase transport effects are neglects. Transport of water occurs by means of vapor motion only. Mazumder and Cole [14] presented a rigorous

* Corresponding author at: University of Science and Technology Beijing, Department of Thermal Engineering, No. 30, Xueyuan Road, Haidian District, Beijing 100083, PR China. Tel.: +86 010 62332730; fax: +86 010 62332730.
E-mail address: liuxl@me.ustb.edu.cn (X. Liu).

3D mathematical model to treat formation and transport of liquid water in PEM. Results show that the inclusion of liquid water transport greatly enhances the predictive capability of the model and is necessary to match experimental data at high current density. Luo et al. [15] presented a three-dimensional, two-phase isothermal model based on the M² model formulation for investigating the condensation and/or evaporation interface, and successfully predicted the important feature of the dry–wet–dry transition in the PEM fuel cell. Zhang et al. [16] studied liquid water transport and its removal from the GDL and gas channel of PEM fuel cells both experimentally and theoretically. Wang and Wang [17] expanded the M² model to permit investigation of the interaction between the two-phase flow and thermal transport due to non-isothermal effects. They also developed an unsteady two-phase model to study the dynamics of the GDL dewetting and its impact on PEM fuel cell performance [18]. A comprehensive two-phase non-isothermal steady model for PEM fuel cell was developed by Basu et al. [19] to investigate two-phase flow and maldistribution in the gas channels.

Recently, other fundamental modeling studies have been reported to investigate water transport phenomena in GDLs based on the Lattice–Boltzmann method [20,21] and the pore-network model [22–24]. Also, experimental investigations have been conducted for the visualization of two-phase flow or quantification of the liquid water content in GDLs within an operating polymer electrolyte fuel cell, using transparent fuel cells [16,25], a fluorescein dye solution [26], and neutron radiography [27–29].

In an earlier publication, our research group has presented an isothermal, three-dimensional comprehensive model of a complete single cell [30]. Phase-change and multiphase flow, however, could not be addressed with that model.

In this paper, a non-isothermal, steady-state, 3D, two-phase, multicomponent transport model is proposed for PEM fuel cell with parallel gas distributors, and numerically solved with a code developed by the authors. In addition to three-dimensionality and the inclusions of both anode and cathode, the present model differs substantially from earlier studies in that the liquid water transport in the electrode and membrane is accounted for via the liquid saturation equation and mass continuity equation, respectively. A detailed membrane model is developed for the liquid water transport with a two-mode water transfer condition, accounting for the non-equilibrium humidification with the replacement of an equilibrium assumption. Also it should be noted that the anode and cathode transport processes are coupled and the water flux balance between anode and cathode sides is insured during the modeling. In the following presentation, the model description will first be stated in detail, including the governing equations and the related boundary conditions, followed by a brief presentation of the numerical algorithm adopted, then detail discussion will be made on the numerical results. Finally some conclusions will be drawn.

2. Model description

The framework of the single-phase PEM fuel cell model in reference [30] is used. A detailed description of the single-phase model has been published and shall not be repeated here. In this paper we focus on modeling of two-phase transport and the prediction of the flooding electrode under operating conditions.

2.1. Model assumptions

In order to make the numerical simulation manageable, some assumptions are to be made as follows.

(1) All phases are assumed to be continuous so that the continuum approach is applicable.

(2) The cell operates under steady-state condition.
(3) The gas mixtures are assumed to be well mixed and can be regarded as the ideal gases. The gas species dissolved in the water is neglected.
(4) The electrode is treated as an isotropic and homogenous porous medium and the properties such as porosity and the permeability are uniform. The membrane is impermeable for gas phase.
(5) Ohmic losses in the GDL and current collector (or bipolar plate) are neglected.
(6) Thermal equilibrium is assumed among gas, liquid and solid phases in the local micro-volume unit of porous electrodes.

2.2. Governing equations

2.2.1. Transport equations of gas mixtures

Generally, the transport of gas mixtures in the flow channels and in the diffusion layers conforms to the mass, momentum, and species conservation principles. The corresponding governing equations are written as follows:

Mass conservation equation

$$\nabla \cdot (\rho \boldsymbol{u}_g) = S_m \tag{1}$$

where $\boldsymbol{u}_g$ is the superficial velocity vector of gas mixture, which is proportional to the intrinsic fluid velocity vector $\boldsymbol{U}$ by the following expression:

$$\boldsymbol{u}_g = \varepsilon(1-s)\boldsymbol{U} \tag{2}$$

where ε is porosity of the porous electrode, and s is the saturation of liquid water indicating the fraction of the void volume occupied by liquid phase in the electrode. In the gas channels, ε is unity and s is zero, then the superficial velocity vector is reduced to the real fluid velocity vector.

Momentum equation

$$\frac{1}{\varepsilon^2(1-s)^2}\nabla \cdot (\rho_g \boldsymbol{u}_g \boldsymbol{u}_g) = -\nabla p_g + \frac{1}{\varepsilon(1-s)}\nabla \cdot (\eta_g \nabla \boldsymbol{u}_g) + \frac{\eta_g}{KK_{rg}}\boldsymbol{u}_g \tag{3}$$

Species mass fraction conservation equations

$$\nabla \cdot (\rho \boldsymbol{u}_g \omega_h) = \nabla \cdot (\rho D_{h,eff} \nabla \omega_h) + S_h \tag{4}$$

$$\nabla \cdot (\rho \boldsymbol{u}_g \omega_o) = \nabla \cdot (\rho D_{o,eff} \nabla \omega_o) + S_o \tag{5}$$

$$\nabla \cdot (\rho_g \boldsymbol{u}_g \omega_w) = \nabla \cdot (\rho_g D_{w,eff} \nabla \omega_w) + S_{w1} + S_{w2} \tag{6}$$

The above governing equations are assumed to be applicable for both flow channel and porous electrode. In these equations, ρ, p and η are the density, pressure and the viscosity of the fluid, respectively; K is the absolute permeability and K_{rg} is the relative permeability for the gas in the porous electrode. The subscript 'g' denotes gas phase. The symbols of ω_h, ω_o and ω_w are the mass fraction of hydrogen, oxygen and water vapor in the gas mixtures, respectively. $D_{i,eff}$ is the effective diffusivity and the subscript 'i' represents the gas species. The last terms existing in Eqs. (1) and (4)–(6) are the volumetric sink or source terms due to the electrochemical reactions or phase change in the electrode, and they are zero in other region of the domain.

Some explanations are given below for the above governing equations. In the general form of momentum equation, Eq. (3), the last term on the right side represents Darcy's drag force imposed by the pore walls on the fluid within the pores, which usually results in a significant pressure drop across the porous medium. It is often called as the micro-scale viscous term or Darcy's viscous term. As indicated above, the general momentum equation is valid in both the porous electrode and the flow channel. In the porous medium, it reduces to the extended Darcy's law for the flow in porous media with a small permeability. While inside the gas channels, it recovers the standard Navier–Stokes equation with the porosity being unity and the permeability being infiniteness.

The effective diffusivity of the species is corrected for flow in the porous media by the so-called Bruggeman model [31]:

$$D_{i,eff} = D_i[\varepsilon(1-s)]^{1.5} \tag{7}$$

where D_i is the diffusivity of gas species in a nonporous system, which is related with the diffusivity under the reference condition expressed by the following expression [32]:

$$D_i = D_{i,ref}\left(\frac{T}{T_{ref}}\right)^{1.5}\left(\frac{p}{p_{ref}}\right)^{-1} \tag{8}$$

The non-zero source terms existing in Eqs. (1) and (4)–(6) for the CLs are given as follows:

Cathode side

$$S_o = -\left(\frac{i_c}{4F}\right)M_o \tag{9}$$

$$S_m = S_o + S_{w1} + S_{w2} \tag{10}$$

Anode side

$$S_h = -\left(\frac{i_a}{2F}\right)M_h \tag{11}$$

$$S_m = S_h + S_{w1} + S_{w2} \tag{12}$$

where i is the local current density in the CL, subscripts 'a' and 'c' denote anode and cathode, respectively, M_h and M_o are the molecular weight of hydrogen and oxygen. The term S_{w1} is the mass transport rate of water between the gas mixture and the humidified membrane. S_{w2} is the mass transport rate of water between the gas phase and liquid phase due to the evaporation and condensation. Their expressions will be given in the following text.

The local current density in anode and cathode is obtained by the Butler–Volmer equation modified by the term considering the liquid water flooding the active reaction sites [7]:

$$i_a = (1-s)A_s j_0^a\left(\frac{c_h^m}{c_{h,ref}^m}\right)^{1/2}\cdot\left\{\exp\left(\frac{\alpha_a n_a F\eta_a}{RT}\right)\right.$$
$$\left.-\exp\left[-(1-\alpha_a)\frac{n_a F\eta_a}{RT}\right]\right\} \tag{13}$$

$$i_c = (1-s)A_s j_0^c\left(\frac{c_o^m}{c_{o,ref}^m}\right)\left\{\exp\left(\frac{\alpha_c n_c F\eta_c}{RT}\right)\right.$$
$$\left.-\exp\left[-(1-\alpha_c)\frac{n_c F\eta_c}{RT}\right]\right\} \tag{14}$$

where j_0 is the exchange current density, η_a and η_c are activation overpotentials of the anode and cathode, respectively, c_h^m and c_o^m are the molar concentrations of hydrogen and oxygen dissolved in the membrane (indicated by the superscript m) phase, respectively, α is the cathode transfer coefficient, n_a is the electron number of anode reaction and n_c is that of cathode reaction.

The dissolved molar concentration of species in the polymer phase is given by Henry's law [33]:

$$c_i^m = Hc_i \tag{15}$$

where H is the Henry constant, c_i and c_i^m are the molar concentrations of species existing in gas phase and membrane phase (or Nafion, polymer phase), respectively, and the subscript i denotes species such as hydrogen or oxygen.

In order to account for the effect of diffusion resistance through the catalyst with porous and agglomerate structure, the local current density is modified by an effectiveness factor θ, which is a measure of how readily reactants diffuse through the catalyst particle [33–36]. This corrected method is so-called the agglomerate model in literatures [34,35]. According to Ref. [36] it can be determined by following equation:

$$\theta = \frac{\tanh M_T}{M_T}, \quad M_T = L_{ct}\sqrt{\frac{k}{D_i^m}} \tag{16}$$

where M_T is called Thiele modulus, L_{ct} denotes the characteristic length of catalyst particle, k is reaction rate constant and D_i^m is species diffusivity of reactant in the polymer phase. An effectiveness factor of 1.0 indicates that reactants diffuse through the agglomerate catalyst particle without resistance. The factor less than 1.0 represents that the agglomerate offers some resistance to reactant diffusion thereby limiting the reaction rate.

2.2.2. Transport equations of liquid water saturation in the electrodes

The above descriptions are for the formulation of the gas mixture transport in the channels and porous electrodes. When water vapor pressure exceeds the saturation level, condensation starts and liquid water exists in the electrode. Inside the porous electrode (including GDL and CL), the liquid water is driven by capillary action. This capillary action is defined as the difference between gas and liquid-phase pressure. Here we give the transport equations of liquid water in the electrodes.

Continuity equation

$$\nabla\cdot(\rho_l \boldsymbol{u}_l) = -S_{w2} \tag{17}$$

where $\boldsymbol{u}_l$ is the superficial velocity vector of the liquid water, subscript 'l' denotes liquid water, and S_{w2} is the mass transport rate of water due to the evaporation and condensation.

Momentum equation

$$\boldsymbol{u}_l = -\frac{K_l}{\eta_l}\nabla p_l \tag{18}$$

The pressure of liquid water is related with the gas pressure by

$$p_c = p_g - p_l = f(s) \tag{19}$$

where p_c is named capillary pressure and is related with liquid water saturation s.

From the above, Eq. (3) can be reduced to the form of Darcy's law in the porous electrode, expressed by

$$\boldsymbol{u}_g = -\frac{K_g}{\eta_g}\nabla p_g \tag{20}$$

The permeability for the liquid and gas phases is represented by

$$K_l = K\cdot K_{rl}, \qquad K_g = K\cdot K_{rg} \tag{21}$$

where K_{rg} and K_{rl} are the relative permeability for the gas and liquid phases, respectively.

Thus, the governing equations for liquid saturation can be induced and rearranged through the substitution to the governing equation (Eq. (17)) with above equations (Eqs. (18)–(21)). The final formulations is expressed as follows:

$$\nabla\cdot\left(\rho_l\frac{\eta_g}{\eta_l}\frac{K_{rl}}{K_{rg}}\boldsymbol{u}_g\right) = \nabla\cdot(\rho_l D_c\nabla s) - S_{w2} \tag{22}$$

where D_c is the capillary diffusion coefficient, written in terms of the following expression:

$$D_c = -\frac{KK_{rl}}{\eta_l}\frac{dp_c}{ds} \tag{23}$$

The empirical model for the relation between p_c and s is written as [37,38]

$$J(s) = \frac{p_c}{\sigma\cos\theta_c}\sqrt{\frac{K}{\varepsilon}} \tag{24}$$

where $J(s)$ is the Leverett's function and σ is the surface tension for the interface between two phases.

The Leverett's function is given by the following relation [11,13,37,38]:

$$J(s) = 1.417(1-s) - 2.120(1-s)^2 + 1.263(1-s)^3 \qquad (25)$$

The relative permeabilities for the gas and liquid phase are assumed to be the cubic function dependent on the relative saturation [39]:

$$K_{rl} = s^3, \qquad K_{rg} = (1-s)^3 \qquad (26)$$

The term S_{w2} is the mass transport rate of water due to the evaporation and condensation. It is determined by [7]

$$S_{w2} = h_m A_s \varepsilon s (\rho_g \omega_{wsat} - \rho_g \omega_w) \qquad (27)$$

where h_m is the mass transfer coefficient of water treated as a constant for simplicity and A_s is the specific area per unit volume of the porous medium. In a sense, the product of h_m and A_s is the same as the parameter called as evaporation rate or condensation rate in Ref. [7]. ε is the dry porosity of the diffusion layer, s is the saturation of liquid water indicating the fraction of the void volume occupied by liquid phase in the porous electrode, and ω_{wsat} is the saturation mass fraction of vapor in the gas mixtures related with the saturation pressure of water, p_{wsat}, which can be fitted to the following empirical expression [3]:

$$\log_{10} p_{wsat} = -2.1794 + 0.02953T - 9.1837 \times 10^{-5}T^2$$
$$+1.4454 \times 10^{-7}T^3 \qquad (28)$$

2.2.3. Transport equations of liquid water in the membrane and CLs

Water transport in the membrane and CLs is governed by the following phenomena: generation of water at the cathode due to the oxygen reduction reaction, forward or backward diffusion of water across the membrane, electro-osmotic drag of water from anode to cathode, and hydraulic permeation due to a hydraulic pressure gradient. It should be noted that the CLs are included in the computational domain, since they are comprised of the ionic phase or Nafion.

From the above, the liquid water flux can be expressed as the following Nernst–Planck equation, similar to the diffusive model proposed by Thampan et al. [40]:

$$N_w = n_d \frac{I}{F} - D_w \nabla c_w - c_w \frac{K_{p,m}}{\eta_l} \nabla p \qquad (29)$$

where N_w is the water molar flux across the membrane, n_d is the electro-osmotic drag coefficient, I is the current density per cross-section area of membrane, F is Faraday constant, c_w is the molar concentration of water in the membrane, D_w is water diffusion coefficient and $K_{p,m}$ is the water permeability in the membrane. In this study, both anode and cathode are operating at 1 atm. Thus the last term related to the pressure difference is omitted.

A mass balance of the water in the membrane and CLs yields

$$\nabla \cdot N_w = 0 \qquad (30)$$

Then the above equation can be rearranged through substitution to it with Eq. (28), as follows:

$$\nabla \cdot (D_w \nabla c_w) - \nabla \cdot \left(n_d \frac{I}{F} \right) = 0 \qquad (31)$$

Note that the sources of water due to electro-osmotic drag with the current have been taken into account by the second term in the above equation.

Several models [8–14] have imposed the condition that the membrane water concentration, at its boundary, is given by the

equilibrium value. However, as discussed in Refs. [41,42], the time scales associated with the water flux in the membrane dominate the relaxation time, in the order of 100–1000 s, required for the membrane to attain its equilibrium hydration state. Thus in the model presented here, the treatment is performed with a two-mode water transfer condition to replace an equilibrium assumption, which is one key feature of the proposed two-phase model.

The membrane water contents are capped at a maximum of water sorption equilibrium. While they are under this maximum value, a water transfer mechanism is assumed as the mass transfer condition and models water transport by a phase-change-like process. The condition takes the form as follows [43,44]

Anodic CL

$$N_{w,a} = -\gamma(c_{w,a} - c^*_{w,a}) \qquad (32)$$

Cathodic CL

$$N_{w,c} = -\gamma(c_{w,c} - c^*_{w,c}) + \frac{I}{2F} \qquad (33)$$

where γ is defined as the water transfer coefficient between the membrane and gases, models mass transfer limitations arising from the GDL and the water transfer into or out of the membrane. c^*_w is the water sorption equilibrium value of molar concentration in the membrane. The term $I/2F$ denotes the produced water in the cathodic CL.

From above, another key feature of this work is that water transport processes of anode and cathode side are coupled and the balance of water flux would be insured between anode and cathode during the modeling. It implies that water molar flux across membrane at the anode side equals to that of cathode side. Fortunately, this is validated in the numerical simulation. In the part of Section 4, the net water fluxes across membrane will be given at different current densities as well as the net water transport coefficient values.

The source term of Eq. (6) S_{w1} is the mass transport rate of water between the gases and the humidified membrane, given as follows

Anodic CL

$$S_{w1} = \gamma(c_{w,a} - c^*_{w,a})\frac{A_{CV}}{V_{CV}} \qquad (34)$$

Cathodic CL

$$S_{w1} = \gamma(c_{w,c} - c^*_{w,c})\frac{A_{CV}}{V_{CV}} \qquad (35)$$

where A_{CV} is the cross-section area of control volume unit and V_{CV} is its volume.

The equilibrium water sorption value in the membrane, denoted by c^*_w, is obtained by the empirical expression [3]:

$$c^*_w = \frac{\rho_{mem,dry}}{M_{mem,dry}} \lambda \qquad (36)$$

where $\rho_{mem,dry}$ and $M_{mem,dry}$ are the density and equivalent weight of a dry proton exchange membrane, respectively. λ is the membrane water content, defined as the moles of water per mole of sulfonic acid sites.

The membrane water content λ of equilibrium hydration state, at both CLs, is given by the following empirical formula [3]:

$$\lambda = 0.043 + 17.81a - 39.85a^2 + 36.0a^3 \quad \text{for } 0 < a \leq 1 \qquad (37)$$

$$\lambda = 14 + 1.4(a - 1) \quad \text{for } 1 \leq a \leq 3 \qquad (38)$$

where a is the water vapor activity of vapor in the gas mixture, defined as

$$a = \frac{x_w p}{p_{sat}} \qquad (39)$$

where x_w is molar fraction of species water vapor and p_{sat} is partial pressure of saturated water.

The water diffusion coefficient in the membrane is based on the literature values [3,45]:

$$D_w = 2.1 \times 10^{-7} \exp\left(\frac{-2436}{T}\right) c_w \tag{40}$$

The electro-osmotic drag coefficient n_d, defined as the number of water molecule carried across the membrane with each hydronium ion, is dependent on the membrane water content λ, given by [5]

$$n_d = 0.0029\lambda^2 + 0.05\lambda - 3.4 \times 10^{-19} \tag{41}$$

2.2.4. Energy equations

In the model assumption, the local thermal equilibrium is maintained in porous medium of the cell. So the solid micro-volume unit and the fluid in the MEA are under the same temperature. Since the liquid water seeps very slowly in the MEA, convective heat transfer due to its transport is neglected. Thus the energy equation takes the form as follows:

$$\nabla \cdot (\rho_g \boldsymbol{u}_g T) = \nabla \cdot (\lambda_{eff} \nabla T) + S_T \tag{42}$$

where λ_{eff} is the effective thermal conductivity and S_T is the source term.

For the porous electrodes, the effective thermal conductivity is calculated by [46]

$$\lambda_{eff} = -2\lambda_s + \frac{1}{\varepsilon/(2\lambda_s + \lambda_g) + (1-\varepsilon)/3\lambda_s} \tag{43}$$

where λ_s and λ_g are the thermal conductivities of carbon paper and the gas mixture, respectively.

In the cathode CL, the heat source is due to entropy changes as well as irreversibility associated with the change transfer [32]:

$$S_T = \left[\frac{T(\Delta S_{re})}{n_c F} + \eta_{c,tot}\right] i_c \tag{44}$$

where ΔS_{re} is the entropy change of cathodic chemical reactions, $\eta_{c,tot}$ is the total cathode overpotential.

In the anode CL, the source term is due to the Ohmic heat effect, given by

$$S_T = \eta_{a,tot} \cdot i_a \tag{45}$$

Table 1
The design and operating parameters of the cell.

Parameters	Value
Gas channel length, L	0.07112 m
Gas channel width, W	7.62×10^{-4} m
Gas channel height, H_{ch}	7.62×10^{-4} m
GDL height, H_d	2.54×10^{-4} m
CL height, H_{ct}	2.87×10^{-5} m
Membrane height, H_m	2.3×10^{-4} m
Inlet temperature, T_{in}	323 K [14]
Anode/cathode pressure, p_a/p_c	1/1 atm [14]
Fuel stoichiometric flow ratio, ζ_a	3
Air stoichiometric flow ratio, ζ_c	3
Relative humidity of inlet fuel, RH_a	100%
Relative humidity of inlet air, RH_c	0
Oxygen mass fraction of inlet air, ω_o	0.232
Electrode porosity, ε	0.4 [2]
Characteristic length of catalyst, L_{ct}	1.0×10^{-6} m [35]

In the membrane, the source term is given by

$$S_T = \frac{I_m^2}{\sigma_m} \tag{46}$$

where I_m is the current density per cross-section area. It is given as follows:

$$I_m = \sigma_m \frac{\partial \phi_m}{\partial z} \tag{47}$$

2.2.5. Electrical potential equations

Two potential equations are solved in the present model to predict solid phase potential ϕ_s and membrane phase potential ϕ_m, which are similar to the framework of the single-phase model and the description is omitted for brief and shall not be repeated here.

2.3. Boundary conditions

The boundary conditions for governing equations of gas mixture transport and electrical potential are similar to the framework of the single-phase model [30]. Thus it is omitted here for brevity. In the above model description, we have discussed the boundary condition for transport equations of liquid water in the membrane and CLs. Here the boundary conditions are only given for liquid saturation equation and energy equation.

Table 2
The physical properties used in the model.

Properties	Value
Electrode permeability, K	1.76×10^{-11} m^2 [2]
Reference diffusivity of H$_2$ in gas, $D_{h,ref}$	0.915 cm^2 s^{-1} (1 atm, 307 K) [32]
Reference diffusivity of O$_2$ in gas, $D_{o,ref}$	0.220 cm^2 s^{-1} (1 atm, 293 K) [32]
Reference diffusivity of H$_2$O in gas, $D_{h,ref}$	0.256 cm^2 s^{-1} (1 atm, 307 K) [32]
Henry constant of H$_2$ in the Nafion, H	0.19 [35]
Henry constant of O$_2$ in the Nafion, H	0.64 [35]
H$_2$ reference concentration, $c_{h,ref}^m$	56.4 mol m^{-3} [2]
O$_2$ reference concentration, $c_{o,ref}^m$	3.39 mol m^{-3} [2]
Diffusivity of O$_2$ in the Nafion, $c_{o,ref}^m$	1.22×10^{-10} m^2 s^{-1} [2]
Diffusivity of H$_2$ in the Nafion, $D_{h,ref}^m$	2.59×10^{-10} m^2 s^{-1} [2]
Cathode transfer coefficient, α	0.5
Exchange current density multiply specific area, anode, $A_s j_0^a$	2.0×10^8 A m^{-3}
Exchange current density multiply specific area, cathode, $A_s j_0^c$	1.6×10^2 A m^{-3}
Characteristic length of catalyst particle, L_{ct}	1.0×10^{-6} m [35]
Density of dry membrane, $\rho_{mem,dry}$	2000 kg m^{-3} [3]
Equivalent weight of dry membrane, $M_{mem,dry}$	1100 kg mol^{-1} [3]
Surface tension, σ	0.0625 N m^{-1} [8]
Water transfer coefficient, γ	5.7×10^{-6} m s^{-1} [43]
Thermal conductivities of bipolar plate, $\lambda_{eff,bp}$	20 W m^{-1} K^{-1} [18]
Thermal conductivities of carbon paper, λ_s	3.0 W m^{-1} K^{-1} [18]
Thermal conductivities of membrane, λ_m	0.95 W m^{-1} K^{-1} [18]
Entropy change of cathodic reactions, ΔS_{re}	326.36 J mol^{-1} K^{-1} [32]
Product of h_m and A_s, $A_s h_m$	160 s^{-1} [7]

At the boundaries between the gas channels and the GDL of anode and cathode, no-slip conditions are implemented for saturation equation.

$$v_l = 0 \tag{48}$$

At the other boundaries, the impermeability conditions are implemented and zero first derivatives are adopted in the normal direction.

As regard to energy equation, the inlet gases temperature is specified by T_{in}. At the outlet of channel, temperature change rates are assumed infinitesimal, i.e. the gradients in the x-direction are set to zero. And adiabatic condition is set for other boundaries.

3. Numerical algorithm and method

The solution to the above governing equations is performed using the finite-volume method [47]. The numerical method is similar to the framework of the single-phase model [30] for gases transport and electrical potential. Thus it is omitted here for the sake of brevity. The flow chart of solution procedure is shown in Fig. 1. Tables 1 and 2 list some parameters and physical properties used in the study.

4. Results and discussion

Major operational parameters of the studied fuel cell are adopted from Refs. [11,14]. Simulations are performed for the operation condition of 323 K and 1/1 atmosphere pressure for anode/cathode. The predicted polarization curve of the cell is shown in Fig. 2. Provided there are also the prediction of single-phase model and experimental data of Ticianelli et al. [48] for comparison purpose. As it can be seen from the figure, a better agreement is achieved by the two-phase model than by the single-phase model. It results from the excessive water flooding of the cathode is taken into account in the two-phase model.

Fig. 3 shows the water vapor mass fraction profiles inside the anode at the average current density of 0.35 A cm^{-2}. Note that as pointed out earlier, the simulations take advantage of the symmetry of the system and only include half of channel and half of the land area. The mass fraction has a small change inside the GDL. This is explained by the fact that consumption of hydrogen leads to a direct increase of the water vapor fraction since the anode gas stream is a binary mixture. But water vapor also could be transported to cathode across the membrane by electro-osmotic drag. Thus there is a small decrease of water vapor concentration along the channel in the anode. It should be noted that the water vapor fraction profile at higher average current density is similar to that shown in Fig. 4. Maybe it is resulted from the above mentioned two factor related to the species mass fraction change.

Fig. 4 shows the water vapor mass fraction profiles inside the cathodic gas diffusion layer at two different average current densities. The dry air flows across the cathode and is humidified by the water produced and transported from anode to cathode. Thus, the mass fraction of water vapor increases along the channel downstream. Inside the cathode of the land area, the reactant gas gains enough humidification by the reason of its small velocity. While at high current density, it would be saturated or over-saturated with vapor (vapor saturation mass fraction is about 9% under atmospheric pressure and operating temperature).

Fig. 5 displays the liquid water content distribution in the membrane under two different average current densities. The liquid water content denotes the moles of water per mole of sulfonic acid sites. It can be seen from the Fig. 5(a) that the water content in anode side is higher than that of cathode from the point of overview under small current density. The inlet reactant in the anode is fully humid-
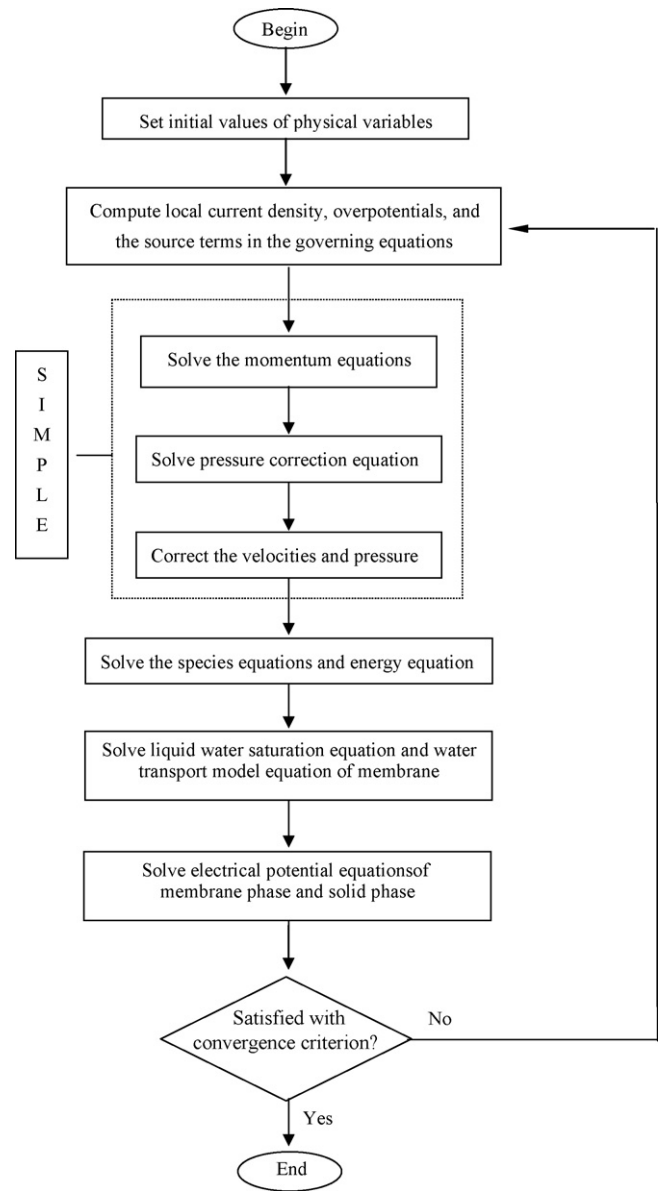

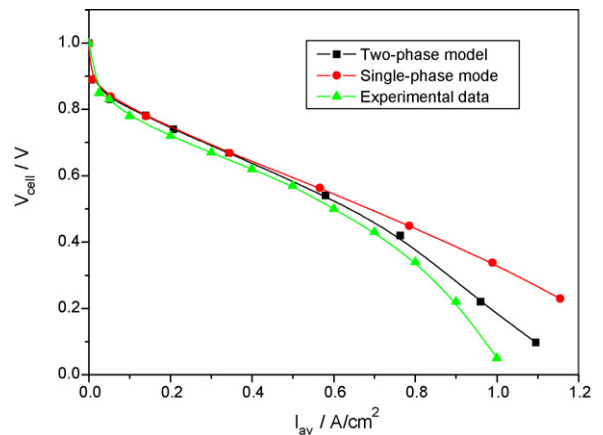Fig. 1. The flow chart of solution procedure.

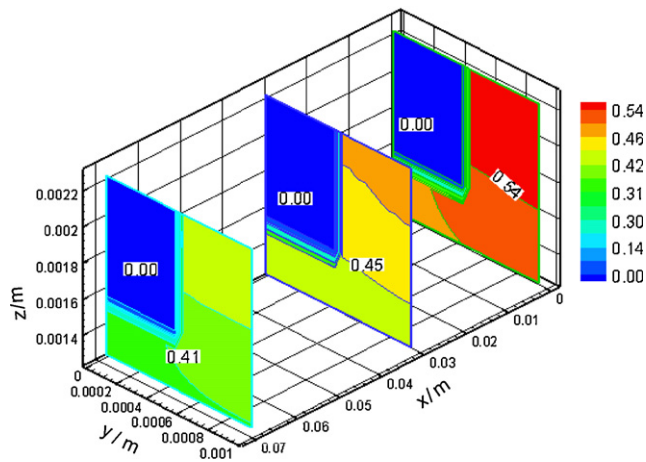Fig. 2. The predicted polarization curve of the cell and the experiment data from Ref. [48].

Fig. 3. Water vapor mass fraction profiles inside the anode under the average current density of $I_{av} = 0.35\,A\,cm^{-2}$.

ified hydrogen. Its relative humidity is decreasing gradually due to the electro-osmotic drag of water from anode to cathode. So the liquid water content in anode side is diminishing in the direction from inlet to outlet, as shown in the Fig. 5(a). However in cathode side, the inlet reactant is dry air. It is humidified by the osmotic water and produced water. The liquid water content of the membrane is higher in the rib-side than in the channel-side, as shown in the Fig. 5(a), by the reason of mass transport limitation. Also the
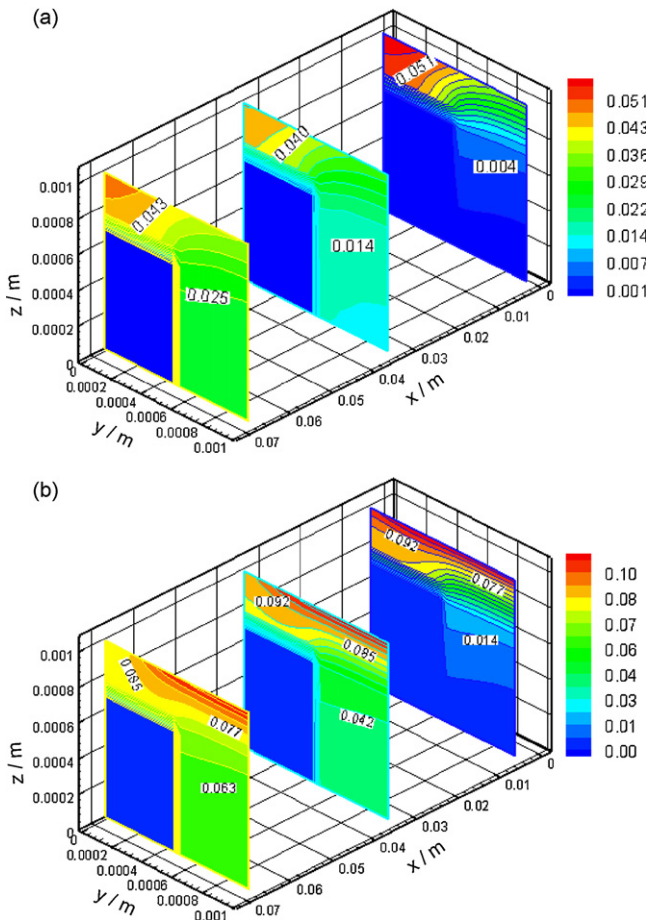

Fig. 4. Water vapor mass fraction profiles inside the cathode under two different average current densities. (a) $I_{av} = 0.35\,A\,cm^{-2}$ and (b) $I_{av} = 1.0\,A\,cm^{-2}$.
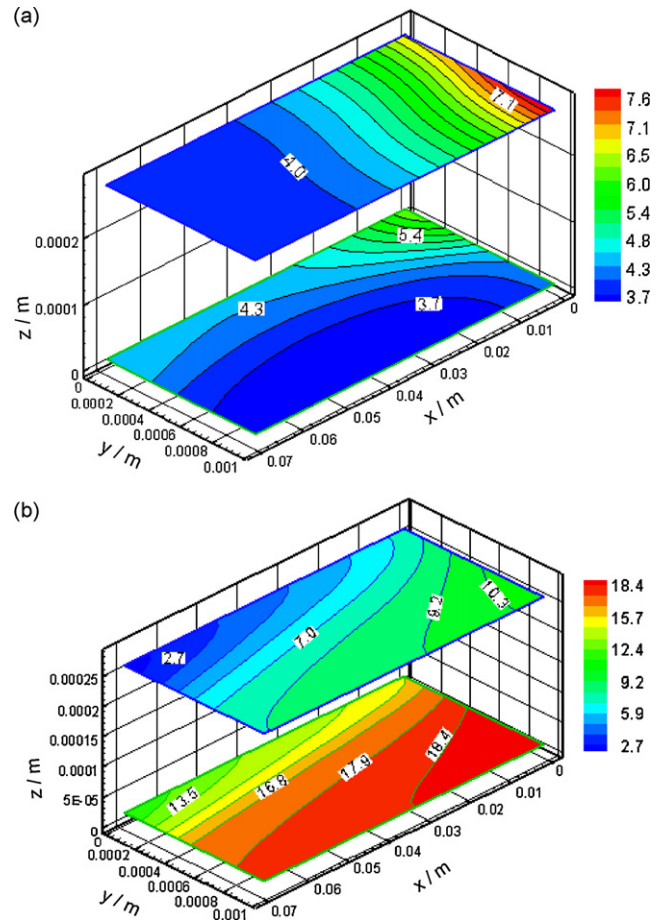

Fig. 5. Liquid water content profiles in the membrane under two different average current densities. (a) $I_{av} = 0.35\,A\,cm^{-2}$ and (b) $I_{av} = 1.0\,A\,cm^{-2}$.

result shows that the liquid water content of anode side is slightly higher than that of cathode side.

However under high current density, liquid water content in the membrane of cathode side is higher than that of the anode side, as can be seen from Fig. 5(b). With the increase of average current density, more water is transported from anode to cathode driven by the electro-osmotic drag. At the same time, a large amount of water is produced and accumulated in the cathodic CL. As a result, liquid water content in the membrane increases under high current density and its values of cathode side are much higher than that of anode side.

It implies that the liquid water diffuses due to the concentration gradient from anode to cathode under low current density. While under high current density, more liquid water diffuses in the reverse direction, i.e. from the cathode to anode.

Fig. 6 displays the liquid water saturation profiles inside cathodic GDL under two different average current densities. When the current density is low, liquid water appears inside cathode of downstream side, and the maximum saturation value is about 7% and located at the rib-side corner of cathode near outlet, as shown in Fig. 6(a). While the current density increases, more liquid water is produced inside cathodic CL by electrochemical reaction and transported to cathode by electroosmosis. As shown in Fig. 6(b), the liquid water saturation increases and distributes in the overall cathodic GDL. The maximum saturation value is about 15%, located at the rib-side of cathodic CL near air inlet. At the upper section near the CL, the liquid water saturation value of rib-side is greater than that of channel-side, which is owing to the nonuniformity of local current density distribution and mass transport limitation. While
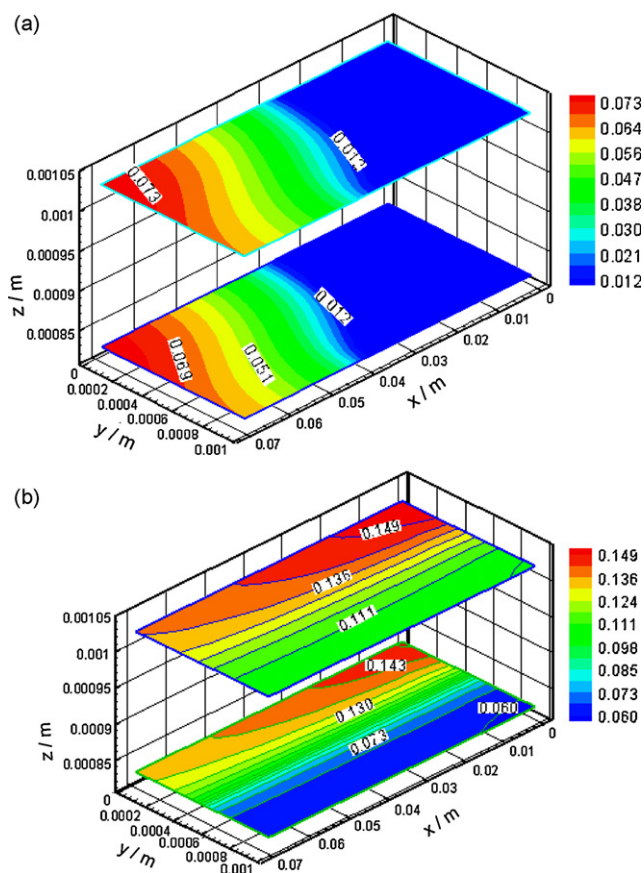
Fig. 6. The liquid water saturation profiles inside cathodic GDL under two different average current densities. (a) $I_{av} = 0.35\,A\,cm^{-2}$ and (b) $I_{av} = 1.0\,A\,cm^{-2}$.

at the lower section of cathodic GDL near the gas channel, the liquid water saturation is less than that of upper section. It should be noted that the form used for the capillary diffusion coefficient D_c has important influence on the liquid water saturation magnitude and its distribution, which is found from our numerical experiments. Also, the boundary conditions for liquid water saturation equation are given coarsely for lack of information, which needs further investigation for the simulation of liquid water saturation.

The velocity field of liquid water inside cathodic GDL is shown in Fig. 7. The liquid water flow occurs in the half part of cathode downstream under small average current density of $0.35\,A\,cm^{-2}$, as shown in Fig. 7(a). The capillary pressure gradient induces the water flow from CL and the GDL into the channel at small average current density. While the current density is high, liquid water flows from the CL and GDL into the channel with greater velocity inside the whole cathode region, as shown in Fig. 7(b). This flow pattern indicates that liquid water inside cathode flows from the place of high liquid water saturation to that of low saturation, which implies that the capillary pressure gradient is the main drive force to induce the liquid water flow inside cathode. The values of the liquid-phase velocity are in the range of $0.2-2 \times 10^{-6}\,m\,s^{-1}$, which are at least three orders of magnitude smaller than that of gas mixtures (about $0.06\,m\,s^{-1}$).

The net water flux through the membrane is often characterized by the parameter β, named after net water transfer coefficient in the literature. It denotes the net amount of water molecules dragged through the membrane per hydrogen proton. Fig. 8 shows the net water flux and the values of β under different densities. The predicted values of β range 0.5 at low current densities to around 0.1 for intermediate current densities in the absence of a pressure gradient. The net water flux
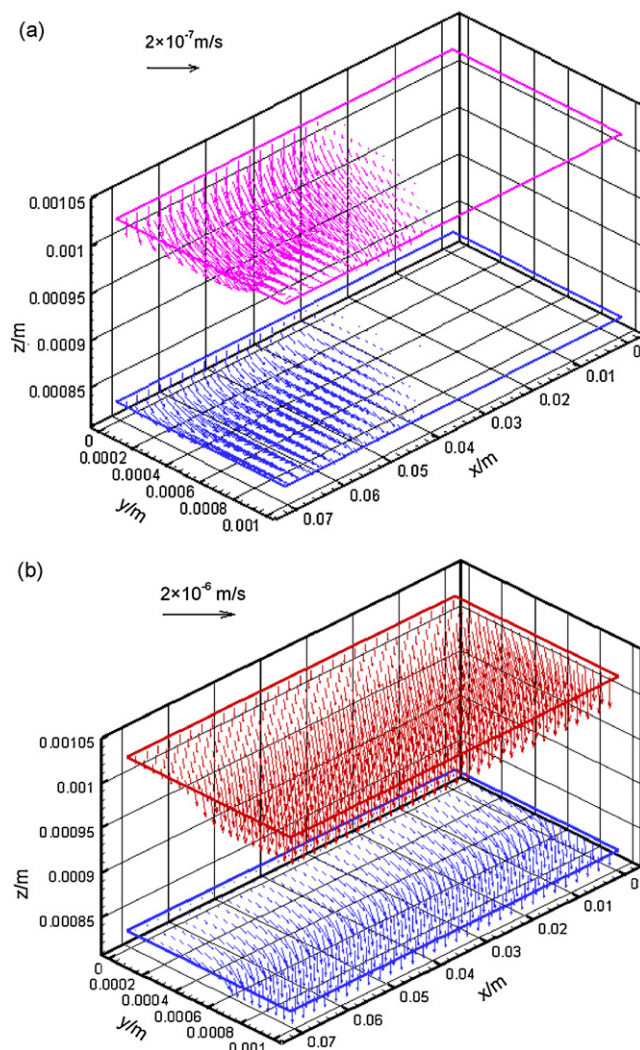

Fig. 7. The velocity field of liquid water inside the cathodic GDL under two different average current densities. (a) $I_{av} = 0.35\,A\,cm^{-2}$ and (b) $I_{av} = 1.0\,A\,cm^{-2}$.

decreases with the increase of current density firstly, which results from the increase of backward diffusion of water across the membrane. The net water flux gets the lowest point under the current density of $0.3\,A\,cm^{-2}$. Then it increases greatly with the increase of current density, since the electro-osmotic drag of
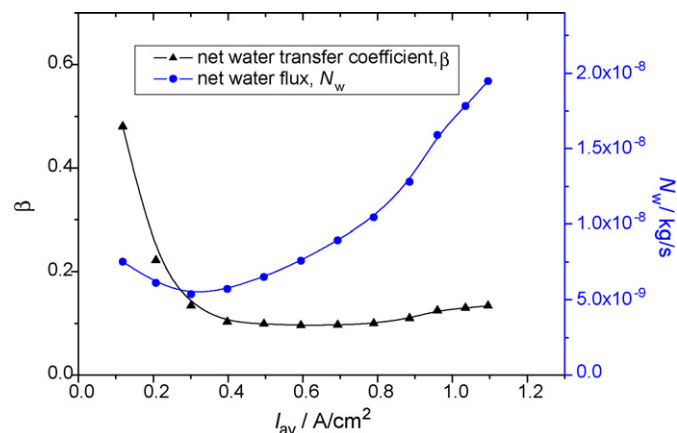

Fig. 8. The net water flux across the membrane and net water transfer coefficient (β) under different densities.
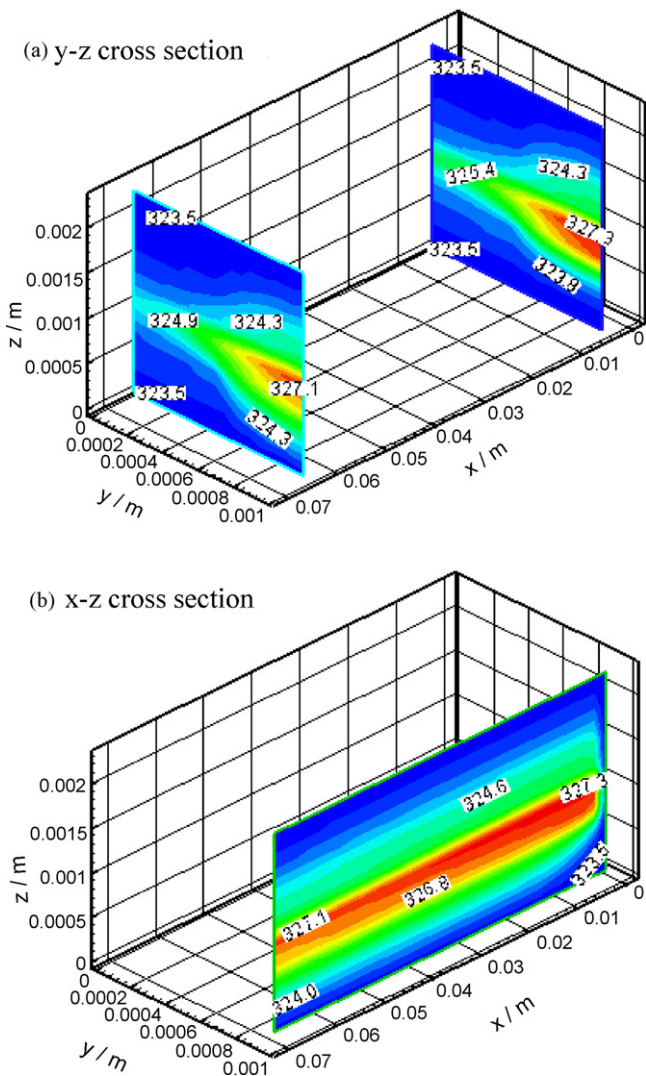
(a) y-z cross section

(b) x-z cross section

Fig. 9. The temperature distribution inside the fuel cell at the average current density of $1.0\,\mathrm{A\,cm^{-2}}$ (a) y–z cross section and (b) x–z cross section.

water from anode to cathode takes the dominant role of water transport.

The temperature distribution inside the fuel cell is shown in the Fig. 9 corresponding to the average current density of $1.0\,\mathrm{A\,cm^{-2}}$. It can be seen from the figure that increase in temperature is about several kelvin in the MEA near the inlet area, where the local current density is highest. Since the features of cathodic electrochemical reaction are different from that of anode, the heat source is mostly generated in the cathodic CL due to the reversible and irreversible entropy production. So the temperature maximum occurs inside the cathodic CL. Due to the low electric conductivity of the membrane, the temperature rise of membrane is higher than that of the GDL. In general, the temperature of the cathode side is slightly higher than that of the anode side.

5. Conclusions

In this work, a non-isothermal, steady-state, three-dimensional, two-phase transport model is developed for PEM fuel cell with parallel gas distributors. The model accounts for liquid water transport processes in the MEA driven by the capillary diffusion, concentration gradient and electro-osmotic drag. A detailed membrane model is developed for the liquid water transport with a two-

mode water transfer condition, accounting for the non-equilibrium humidification of membrane with the replacement of an equilibrium assumption, which is a key feature of this model. Another key feature is that the anode and cathode transport are coupled and the water flux balance is insured between anode and cathode during the modeling.

The model is validated by comparison between the simulated results and available experimental data, and good agreement is achieved. The simulations are performed for water vapor concentration field, membrane water content distribution, liquid water flow field and saturation distribution inside the cathode, and temperature field inside the cell. Three-dimensional effects are found to play a significant role in determining local distribution, even for the relatively simple fuel cell geometry considered here.

For the studied case with dry cathode and saturated anode condition, the major findings of this paper can be summarized as follows.

(1) The water content in the membrane of anode side is higher than that of the cathode side under small current density, whereas lower under higher current density. It implies that the liquid water diffuses due to the concentration gradient in the different direction under different current densities.
(2) Liquid water appears originally in the cathode near outlet under small current density. The liquid water flows from the CL and GDL toward the gas channel induced by liquid water saturation gradient. Its velocity is at least three orders of magnitude smaller than that of the gas mixtures.
(3) The predicted values of the net water transfer coefficient range from 0.5 at low current densities to around 0.1 for intermediate current densities in the absence of a pressure gradient. The net water flux decreases with the increase of current density first and reaches the lowest point under the average current density of $0.3\,\mathrm{A\,cm^{-2}}$. Then it increases smoothly with the increase of current density.
(4) The maximum temperature inside the cell is located at the cathodic CL near the inlet and the maximum temperature rise is about several degrees in the cell. The temperature of cathode side is slightly higher than that of anode side.

Nomenclature

A_s	specific reaction area of the catalyst layer $(\mathrm{m^{-1}})$
A_{ch}	inlet channel cross-section area $(\mathrm{m^2})$
A_m	geometrical area of the membrane $(\mathrm{m^2})$
c	molar concentration $(\mathrm{mol\,m^{-3}})$
D	mass diffusivity $(\mathrm{m^2\,s^{-1}})$
F	Faraday constant $(96{,}487\,\mathrm{C\,mol^{-1}})$
h_m	mass transfer coefficient of water $(\mathrm{m\,s^{-1}})$
H	height (m); Henry constant (dimensionless)
i	volumetric current density $(\mathrm{A\,m^{-3}})$
I	average current density $(\mathrm{A\,m^{-2}})$
j_0	exchange current density $(\mathrm{A\,m^{-2}})$
K	permeability of electrode $(\mathrm{m^2})$
$K_{p,m}$	water permeability in the membrane $(\mathrm{m^2})$
L	length (m)
M	molecular weight (dimensionless)
M_T	Thiele modulus (dimensionless)
N_w	water molar flux across the membrane $(\mathrm{kg\,s^{-1}})$
n_d	electro-osmotic drag coefficient (dimensionless)
p	pressure (Pa)
R	universal gas constant $(8.3145\,\mathrm{J\,mol^{-1}\,K^{-1}})$
s	liquid water saturation (dimensionless)
S	source term of equations

ΔS_{re}	entropy change of cathodic chemical reactions ($\mathrm{J\,mol^{-1}\,K^{-1}}$)
T	temperature (K)
v	velocity vector ($\mathrm{m\,s^{-1}}$)
V	electrical potential (V)
x	coordinate (m)
y	coordinate (m)
z	coordinate (m);

Greek letters

α	transfer coefficient of electrochemical reaction (dimensionless)
β	net water transport coefficient per proton (dimensionless)
ϕ	electrical potential (V)
σ	electrical conductivity ($\mathrm{S\,m^{-1}}$), surface tension ($\mathrm{N\,m^{-1}}$)
γ	water transfer coefficient ($\mathrm{m\,s^{-1}}$)
ε	porosity of electrode (dimensionless)
η	viscosity ($\mathrm{kg\,m^{-1}\,s^{-1}}$); overpotential (V)
λ	thermal conductivity ($\mathrm{W\,m^{-1}\,K^{-1}}$)
ρ	density ($\mathrm{kg\,m^{-3}}$)
ζ	stoichiometric flow ratio (dimensionless)
ω	species mass fraction (dimensionless)

Subscripts

av	average
a	anode
bp	bipolar plate
c	cathode, capillary
ct	catalyst
ch	channel
d	dry
eff	effective
g	gas
i	species
in	inlet
l	liquid
m	membrane, mass
max	maximum momentum
mem	membrane
o	oxygen
r	relative
ref	reference values
s	solid; specific
sat	saturation
tot	total
w	water

Superscripts

a	anode
c	cathode
m	membrane

Acknowledgment

References

[1] D.M. Bernardi, M.W. Verbrugge, AIChE J. 37 (8) (1992) 1151–1163.
[2] D.M. Bernardi, M.W. Verbrugge, J. Electrochem. Soc. 139 (9) (1992) 2477–2491.
[3] T.E. Springer, T.A. Zawodzinski, S. Gottesfeld, J. Eletrochem. Soc. 138 (8) (1991) 2334–2342.
[4] T.E. Fuller, I. Newman, J. Eletrochem. Soc. 146 (1998) 1218–1225.
[5] T.V. Nguyen, R.E. White, J. Electrochem. Soc. 140 (8) (1993) 2178–2186.
[6] J.J. Baschuk, X. Li, J. Power Sources 86 (2000) 181–196.
[7] W. He, J.S. Yi, T.V. Nguyen, AIChE J. 46 (10) (2000) 2053–2064.
[8] Z.H. Wang, C.Y. Wang, K.S. Chen, J. Power Sources 94 (2001) 40–50.
[9] C.Y. Wang, P. Cheng, Int. J. Heat Mass Transfer 39 (17) (1996) 3607–3632.
[10] L. You, H.T. Liu, Int. J Heat Mass Transfer 45 (2002) 2277–2287.
[11] T. Berning, N. Djilali, J. Electrochem. Soc. 150 (12) (2003) A1589–A1598.
[12] S. Dutta, S. Shimpalee, J.W. Van Zee, J. Appl. Electrochem. 30 (2000) 135–146.
[13] S. Dutta, S. Shimpalee, J.W. Van Zee, Int. J. Heat Mass Transfer 44 (2001) 2029–2042.
[14] S. Mazumder, J.V. Cole, J. Electrochem. Soc. 150 (11) (2003) A1510–A1517.
[15] G. Luo, H. Ju, C.Y. Wang, J. Electrochem. Soc. 154 (3) (2007) B316–B321.
[16] F.Y. Zhang, X.G. Yang, C.Y. Wang, J. Electrochem. Soc. 153 (2) (2006) A225–A232.
[17] Y. Wang, C.Y. Wang, J. Electrochem. Soc. 153 (6) (2006) A1193–A1200.
[18] Y. Wang, C.Y. Wang, J. Electrochem. Soc. 154 (2007) B636–B643.
[19] S. Basu, J. Li, C.Y. Wang, J. Power Sources 187 (2009) 431–443.
[20] J. Park, X. Li, J. Power Sources 178 (2008) 248–257.
[21] Y. Tabe, Y. Lee, T. Chikahisa, M. Kozakai, J. Power Sources 193 (2009) 24–31.
[22] P.K. Sinha, C.Y. Wang, Electrochim. Acta 52 (2007) 7936–7945.
[23] A. Bazylak, V. Berejnov, B. Markicevic, D. Sinton, N. Djilali, Electrochim. Acta 53 (2008) 7630–7637.
[24] K.J. Lee, J.H. Nam, C.J. Kim, Electrochim. Acta 54 (2009) 1166–1176.
[25] H. Masuda, K. Ito, T. Oshima, K. Sasaki, J. Power Sources 177 (2008) 303–313.
[26] S. Litster, D. Sinton, N. Djilali, J. Power Sources 154 (2006) 95–105.
[27] D. Kramer, J.B. Zhang, R. Shimoi, E. Lehmann, A. Wokaun, K. Shinohara, G.G. Scherer, Electrochim. Acta 50 (2005) 2603–2614.
[28] M.A. Hickner, N.P. Siegel, K.S. Chen, D.S. Hussey, D.L. Jacobson, M. Arif, J. Electrochem. Soc. 155 (2008) B427–B434.
[29] C. Hartnig, I. Manke, R. Kuhn, S. Kleinau, J. Goebbels, J. Banhart, J. Power Sources 188 (2009) 468–474.
[30] X.L. Liu, W.Q. Tao, Z.Y. Li, Y.L. He, J. Power Sources 158 (1) (2006) 25–35.
[31] N.P. Siegel, M.W. Ellis, D.J. Nelson, M.R. Spakovsky, J. Power Sources 128 (2004) 173–184.
[32] T. Berning, D.M. Lu, N. Djilali, J. Power Sources 106 (2002) 284–294.
[33] K. Broka, P. Ekdunge, J. Appl. Electrochem. 27 (1997) 281–289.
[34] Y. Bultel, P. Ozil, R. Durand, J. Appl. Electrochem. 28 (1998) 269–276.
[35] N.P. Siegel, M.W. Ellis, D.J. Nelson, M.R. von Spakovsky, J. Power Sources 115 (2003) 81–89.
[36] O. Levenspiel, Chemical Reaction Engineering, third edition, John Wiley Son Pte Ltd, Delhi, 1999.
[37] M.C. Leverett, Trans. AIME 142 (1941) 152–169.
[38] U. Pasaogullari, C.Y. Wang, J. Electrochem. Soc. 151 (3) (2004) A399–A406.
[39] M. Kaviany, Principles of Heat Transfer in Porous Media, Springer, New York, 1991.
[40] T. Thampan, S. Malhotra, H. Tang, R. Datta, J. Electrochem. Soc. 147 (2000) 3242–3250.
[41] V.I. Basura, Electrochemistry of proton exchange membranes [D]. Ph.D. Thesis, Simon Fraser University, Burnaby, Canada, 2000.
[42] F. Opekar, D. Svozil, J. Electroanal. Chem. 385 (1995) 269–281.
[43] P. Berg, K. Promislow, J.S. Pierre, J. Stumper, B. Wetton, J. Electrochem. Soc. 151 (3) (2004) A341–353.
[44] R. Krishna, R. Taylor, Mulicomponent Mass Transfer, Wiley, New York, 1993.
[45] S.S. Motupally, A.J. Becker, J.W. Weidner, J. Electrochem. Soc. 147 (2000) 3171–3177.
[46] V. Gurau, H. Liu, K. Sadik, AIChE J. 44 (11) (1998) 2410–2422.
[47] W.Q. Tao, Numerical Heat Transfer, second edition, Xi'an Jiaotong Univ. Press, Xi'an, 2001.
[48] E.A. Ticianelli, J.G. Berry, S. Srinivasan, J. Electroanal. Chem. 251 (1988) 275–295.